Tailoring of electronic and surface structures boosts exciton-triggering photocatalysis for singlet oxygen generation

Dongpeng Zhang[a,1], Pengfei Wang[b,1], Junhui Wang[c,1], Yanxiao Li[a], Yuguo Xia[d], and Sihui Zhan[a,2]

[a]Ministry of Education Key Laboratory of Pollution Processes and Environmental Criteria/Tianjin Key Laboratory of Environmental Remediation and Pollution Control, College of Environmental Science and Engineering, Nankai University, Tianjin 300071, China; [b]Tianjin Key Lab Clean Energy & Pollutant Control, School of Energy and Environmental Engineering, Hebei University of Technology, Tianjin 300130, China; [c]State Key Laboratory of Molecular Reaction Dynamics, Dalian Institute of Chemical Physics, Chinese Academy of Sciences, Dalian 116023, China; and[d]School of Chemistry and Chemical Engineering, Shandong University, Shandong 250100, China

Edited by Alexis T. Bell, University of California, Berkeley, CA, and approved October 25, 2021 (received for review August 10, 2021)

Arising from reduced dielectric screening, excitonic effects should be taken into account in ultrathin two-dimensional photocatalysts, and a significant challenge is achieving nontrivial excitonic regulation. However, the effect of structural modification on the regulation of the excitonic aspect is at a comparatively early stage. Herein, we report unusual effects of surface substitutional doping with Pt on electronic and surface characteristics of atomically thin layers of Bi_3O_4Br, thereby enhancing the propensity to generate $^1O_2$. Electronically, the introduced Pt impurity states with a lower energy level can trap photoinduced singlet excitons, thus reducing the singlet–triplet energy gap by ∼48% and effectively facilitating the intersystem crossing process for efficient triplet excitons yield. Superficially, the chemisorption state of O_2 causes the changes in the magnetic moment (i.e., spin state) of O_2 through electron-mediated triplet energy transfer, resulting a spontaneous spin-flip process and highly specific $^1O_2$ generation. These traits exemplify the opportunities that the surface engineering provides a unique strategy for excitonic regulation and will stimulate more research on exciton-triggering photocatalysis for solar energy conversion.

photocatalysis | regulation of exciton | $^1O_2$ generation | O_2 activation | organic degradation

Rapid economic growth is exhausting the traditional fossil fuel supply, which causes the global threat of climate change from an increase of greenhouse gas emissions. To enable a carbon-neutral industrial society, utilizing sustainable and clean solar energy to meet the increasing energy demand has been considered to be the most viable choice (1). Among the effective solar energy utilization routes (i.e., photothermal, photovoltaic, and photocatalytic approaches) (2), semiconductor-based photocatalysis has triggered broadened research activity and shows a promising prospect for photoreforming (3) and environmental remediation (4) from sunlight. Recently, ultrathin two-dimensional photocatalysts have been widely employed in diverse photocatalytic energy exploitation because of their optimized electronic and surface properties (5). Nevertheless, the traditional viewpoints of photogenerated excited species (i.e., free charge carriers) in ultrathin two-dimensional photocatalysts are always incomprehensive. From bulk (or multilayer) to ultrathin (especially monolayer) structures, photocatalysts can experience reduced dielectric screening, and thus the excitons (or bound electron–hole pairs) might be the dominant species due to the enlarged excitonic binding energy (E_b) (6). In this case, the exciton-based resonance energy transfer can selectively active triplet oxygen (O_2) to highly reactive singlet O_2 ($^1O_2$) for, but not limited to, selective organic synthesis, wastewater treatment, and photodynamic therapy (7). Although gaining a deeper understanding of the excitonic effect is beneficial to reveal the complex photocatalytic mechanism, it has been long ignored, and up to now quite limited optimization strategies have been proposed to regulate the excitonic processes.

A typical O_2 activation in the charge-carrier-involved photocatalytic reaction primarily comprises photoabsorption, electron–hole separation, and O_2 reduction by photoexcited electrons; the first two steps are closely related to the electronic structure, while the third is mainly determined by the surface structure (8). To regulate the factors overall, a major and versatile tool is surface defect (usually atomistic doing and vacancy) engineering (9). First, the defects can effectively narrow the bandgap to extend the light absorption to visible (∼43% of the solar spectrum) or near-infrared (∼52% of the solar spectrum) regions (10). Moreover, the defects can induce new electronic states, denoted as "trap states" or "surface states" within the bandgap, which can capture photoexcited electrons or holes to enable charge carrier separation (11). Finally, the surface defects also can serve as the active sites for O_2 chemisorption and spatially supply channels for electron transfer (12). Benefiting from the mentioned charge regulation processes, defect-induced photocatalysts can generate more superoxide ($O_2^{\bullet-}$), as schematically illustrated in Fig. 1*A*.

Despite tremendous efforts devoted to free charge regulation in charge-carrier-involved semiconductors, surface defect in exciton-involved two-dimensional semiconductors is at a comparatively early stage, and the resultant effects are less explored. With a conventional energy band model in excitonic processes,

Significance

As the dielectric confinement effects in ultrathin two-dimensional photocatalysts, excitonic effects originating from the Coulomb interactions between photogenerated electrons and holes can be significantly promoted, which would endow the systems with distinct photoexcitation scenarios. A significant challenge is achieving nontrivial excitonic regulation, especially for inorganic semiconductors, to efficiently use solar energy. This research presents a strategy of modifications in both electronic and surface structures caused by surface Pt dopants to enhance the propensity to generate $^1O_2$ by triplet energy transfer. This design concept highlights a promising exciton control strategy in two-dimensional inorganic semiconductors and demonstrates the importance of impurity states in the energy transfer process.

Author contributions: D.Z., P.W., and S.Z. designed research; D.Z. performed research; D.Z., J.W., Y.L., and Y.X. analyzed data; and D.Z., P.W., and S.Z. wrote the paper.

The authors declare no competing interest.

This article is a PNAS Direct Submission.

[1]D.Z., P.W., and J.W. contributed equally to this work.

[2]To whom correspondence may be addressed. Email: sihuizhan@nankai.edu.cn.

This article contains supporting information online at http://www.pnas.org/lookup/suppl/doi:10.1073/pnas.2114729118/-/DCSupplemental.

Published November 22, 2021.

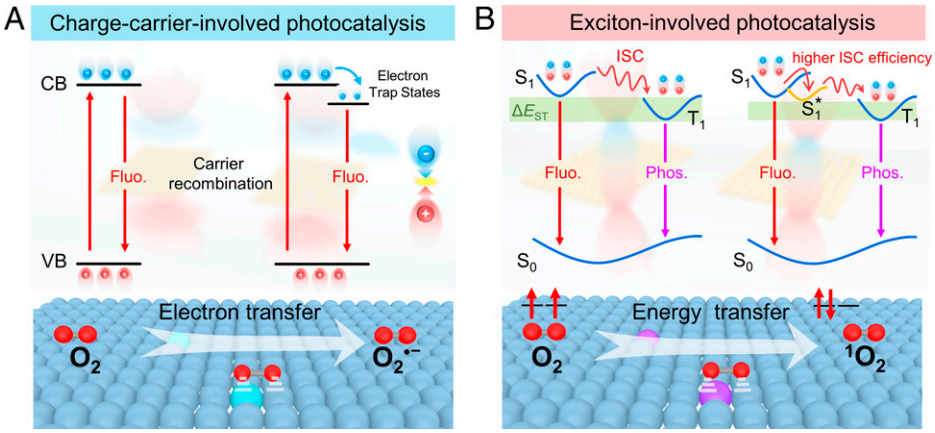

Fig. 1. Schematic description of the manipulation of electronic and surface structures in different photocatalytic systems by inducing surface defects. (*A*) The charge-carrier-involved photocatalytic reaction with "electron trap states" for carrier separation and surface O_2 chemisorption for $O_2^{\bullet-}$ generation. (*B*) The exciton-involved photocatalytic reaction with "singlet-excitons trap states" and surface O_2 chemisorption for $^1O_2$ generation. Fluo., fluorescence; Phos., phosphorescence; CB, conduction band; VB, valence band.

the electrons at conduction band minimum and the holes at valence band maximum can form singlet excitons (S_1), which then return to the ground state (S_0), accompanied by fluorescence. Excitons in S_1 can also undergo intersystem crossing (ISC) to lower-energy triplet excited states (T_1). Then, the energy transfer between excitons in T_1 and O_2 in S_0 can generate $^1O_2$, accompanied by phosphorescence (13). In this regard, the rich triplet-excitons yield of photocatalysts is responsible for enhanced $^1O_2$ generation. Inspired by the overall regulation of O_2 activation in charge-carrier-involved photocatalytic reaction, we speculate that modulation of surface defects may enhance triplet-excitons yield and $^1O_2$ generation (as illustrated in Fig. 1*B*). First, the singlet exciton concentrations in semiconductors are typically linked to binding energies (E_b), which exhibit prominent dependence on size and/or thickness (14), and thus an ultrathin structure (even monolayer) is an essential prerequisite, especially for inorganic semiconductors. Second, to generate more triplet excitons, a higher ISC efficiency is needed, which can be largely influenced by singlet–triplet energy gap (ΔE_{ST}) (15). Thus, inducing a lower singlet-excitons trap energy level (S_1^*) by surface defect engineering would efficiently reduce ΔE_{ST} and inhibit its fast relaxation. Finally, on the surface reaction side, a density functional theory (DFT) study reported evidence for unnecessary direct contact between O_2 and catalysts (16), but this is still under debate because another study interpreted that chemisorption O_2 to the catalysts can tune $^1O_2$ generation (17).

In this work, we designed and synthesized modifications in both electronic and surface structures caused by Pt dopants in Bi_3O_4Br single-unit-cell layers to validate our hypothesis. We chose to investigate an inorganic catalyst to explore how dopants influence the excitonic processes, because it is very difficult to distinguish the complicated surface structures of polymer photocatalysts, which would confuse the unraveling of the energy transfer and O_2 activation. We show that doping-induced electronic restructuring can form new impurity-mediated singlet exciton trap states (TS) to facilitate ISC processes, leading to the enhancement of triplet-excitons generation. Meanwhile, the modified surface structure can change the bonding configurations between photocatalysts and O_2, which is beneficial to O_2 chemisorption and energy transfer.

Results

Materials Synthesis and Characterization. The Bi_3O_4Br single-unit-cell layer was prepared via surfactant self-assembly strategy (18), and in light of the ultrathin structure we reasoned that it should be a promising candidate to study the excitonic regulation (denoted as EBOB) (19). The Pt-doped Bi_3O_4Br single-unit cell was synthesized by a facile liquid-phase reaction method (*SI Appendix*, Fig. S1), and four representative doping concentrations were chosen: 0.3, 0.5, 0.7, and 1% (where the percent is defined as the mass fraction of Pt). Among all the samples, the sample with 0.7% Pt loading shows the best activity, and hence it was chosen as the model catalyst in this study (denoted as EBOB:Pt). The X-ray diffraction (XRD) in Fig. 2*A* and Raman spectra in *SI Appendix*, Fig. S2 suggest the successful preparation of orthorhombic EBOB and EBOB:Pt without the appearance of any impurity phase. The transmission electron microscopy (TEM) image (*SI Appendix*, Fig. S3) and atomic force microscopy (AFM) image (Fig. 2*B*) show a sheet-like morphology of EBOB:Pt with an average thickness of ~1.90 nm, agreeing with the single-unit-cell thickness of Bi_3O_4Br (*c* parameter) (20). The atomic resolution high-angle annular dark-field scanning TEM (HAADF-STEM) image (Fig. 2 *C* and *D*) and selective area electron diffraction (*SI Appendix*, Fig. S4) confirm the single crystalline and the [001] orientation of EBOB:Pt. Note that the brightness of atom column in HAADF-STEM is dependent on the atomic number, and the brightness level of atoms should be Bi (83) > Pt (78) (21). Thus, the fine distribution and arrangement of Pt in EBOB can be determined. As shown in Fig. 2*D* and the corresponding atomic model (Fig. 2*E*), some darker Pt atoms are atomically dispersed on the EBOB (001) surface. As further analyzed by the selected-area intensity surface plot (Fig. 2*F*1) and line intensity profile (Fig. 2*F*2), the isolated Pt atoms are substituting Bi atoms in the crystal lattice. In addition, elemental mapping (Fig. 2*G*) shows a uniform distribution of Pt. In addition, to better understand the exciton regulation of Pt doping, the bulk Bi_3O_4Br was also synthesized to serve as charge-carrier-involved control group (denoted as CBOB), and the corresponding 0.7% Pt substitution doping (denoted as CBOB:Pt) has been determined (*SI Appendix*, Figs. S5 and S6).

To further disclose the atomic structure of Pt, X-ray photoelectron spectrometry (XPS) and synchrotron radiation-based X-ray absorption spectroscopy were performed. *SI Appendix*, Fig. S7 shows the Pt 4f core level of Pt/C and EBOB:Pt. Notably, the Pt $4f_{7/2}$ and $4f_{5/2}$ orbitals of CBOB:Pt shift to higher binding energies, which indicate Pt atoms with partially positive charge ($Pt^{\delta+}$) owing to the electronic interaction between Pt atoms and EBOB (22). Pt L_3-edge X-ray absorption near-edge structure (XANES) was further used to confirm the valence state of Pt. As shown in Fig. 3*A*, the absorption edge position

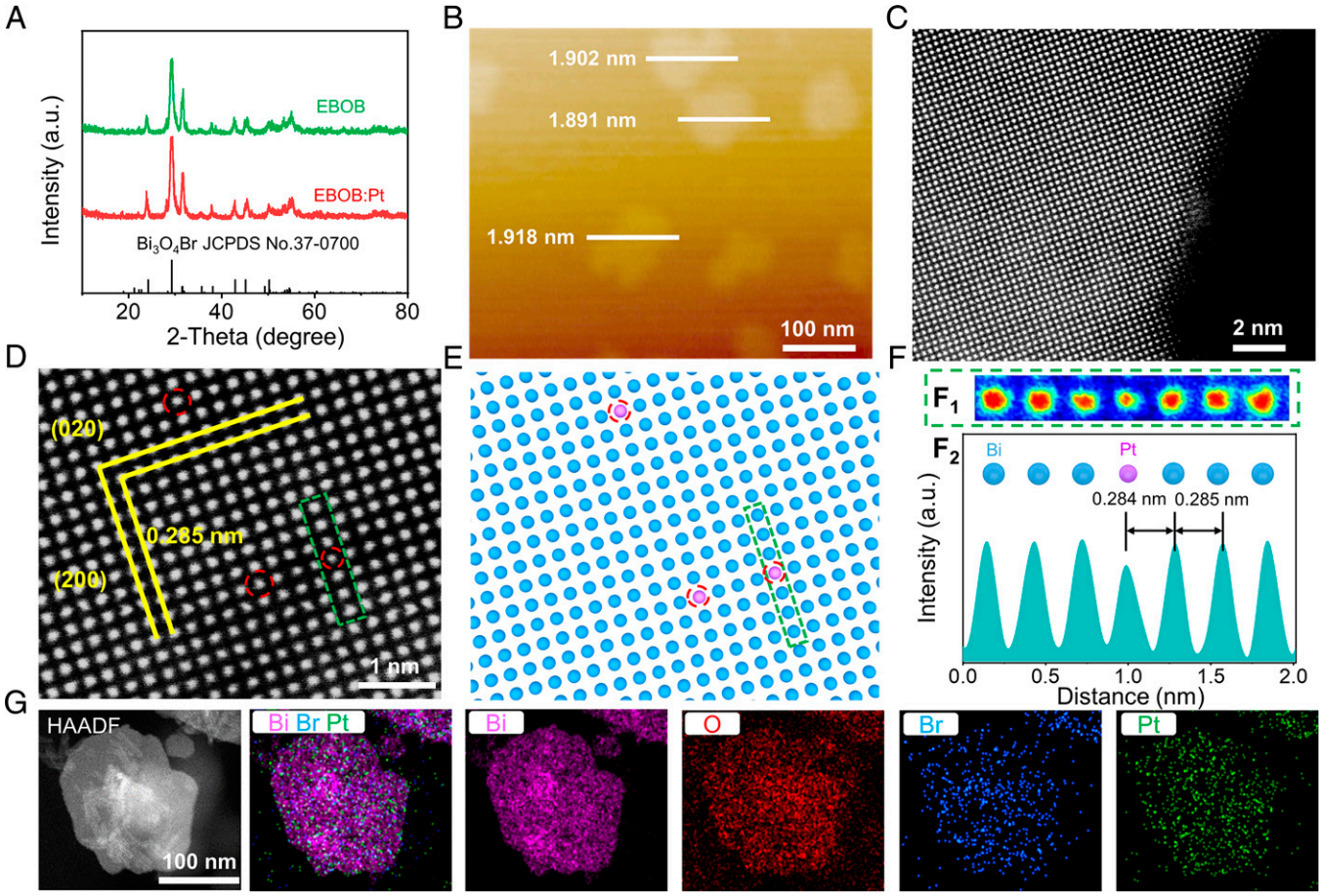

Fig. 2. Surface structural characterizations of Pt substituted Bi_3O_4Br single-unit-cell layers. (*A*) XRD patterns of EBOB:Pt and pristine EBOB. (*B*) AFM image showing the average thickness of EBOB:Pt. (*C* and *D*) Atomic resolution HAADF-STEM of EBOB:Pt. (*E*) The corresponding atomic model of *D*. (*F*) Intensity surface plot (F_1) and line intensity profiles (F_2) taken from the selected area (green dashed rectangle) in *D*. (*G*) HAADF-STEM and the corresponding elemental images of EBOB:Pt. a.u., arbitrary units.

of EBOB:Pt is located between those of the Pt foil and PtO_2, suggesting that the oxidation state of Pt atoms is between 0 and +4. Also, the white-line intensity of EBOB:Pt further confirms its valence state is ~+2.95, implying that Bi^{3+} might be substituted. Then, extended X-ray absorption fine structure (EXAFS) was carried out to gain insight into the atomic coordination structure of Pt. Viewed from the Fourier-transformed (FT) k^2-weighted EXAFS spectra (Fig. 3*B* and *SI Appendix*, Fig. S8*A*), EBOB:Pt does not emerge the peak of Pt–Pt bond in reference to standard Pt foil and PtO_2, confirming the absence of Pt or PtO_2 clusters or particles. Also, the sole FT peak located at 1.49 A° is attributed to the coordination with O atoms in the EBOB lattice (20). To further confirm this inference, the Pt L-edge wavelet transform (WT)-EXAFS, as the powerful resolution in both *k* and *R* spaces, was applied. In Fig. 3*C*, the WT contour plot of EBOB:Pt shows a maximum at ~4 $A^{\circ -1}$, owing to the Pt-O contribution. Compared to the WT contour plot of the Pt foil, there is no intensity maximum detected near 8.5 $A^{\circ -1}$, further confirming the atomically dispersed Pt atom. Quantitatively, the structural parameters at the Pt L-edge were extracted by least-square EXAFS fitting (Fig. 3*D* and *SI Appendix*, Fig. S8 and Table S1), and the fitting curve matches quite well with the experiment spectra. As indicated by the results, the first shell of the central atom Pt displays a coordination number of 3.96, directly connect by four O atoms, with mean bond lengths of 2.001 A°. All these results qualitatively verify the distinct local atomic arrangement of EBOB:Pt (Fig. 3*F*), and this is also validated by the 0.2-eV upshift of the Bi 4f XPS peak relative to that of EBOB (Fig. 3*E*), which is attributed to the higher electronegativity of Pt compared to Bi (10). Similarly, the coordination environment of Pt atoms in the CBOB systems has also been analyzed, which confirms the Pt atoms are substituting Bi atoms in the crystal lattice (*SI Appendix*, Figs. S9 and S10 and Table S2).

Molecular Oxygen Activation Tests. To distinguish the different photogenerated species in EBOB and CBOB, we first identified the reactive oxygen species (ROS) in different systems, as generation of superoxide ($O_2^{\bullet -}$), hydroxyl radicals (•OH), and hydrogen peroxide (H_2O_2) are related to electrons and holes, while singlet oxygen ($^1O_2$) is related to the triplet energy transfer process (19). Herein, 3,3',5,5'-tetramethylbenzidine (TMB) was used the probe molecule to detect the O_2 activation, in which the absorbance peak at 380 nm suggests the oxidation of TMB (*SI Appendix*, Fig. S11). Then, various scavengers including superoxide dismutase (SOD), mannitol, catalase, and carotene were introduced to investigate their specific influences on $O_2^{\bullet -}$, •OH, H_2O_2, and $^1O_2$, respectively. As shown in Fig. 4*A*, carotene is found to suppress TMB oxidation for EBOB and EBOB:Pt, suggesting $^1O_2$ to be the major ROS. Meanwhile, a little $O_2^{\bullet -}$ also exists in the EBOB system, implying its instability of excitons and the excitons may dissociate to free electrons and holes (6). In sharp contrast, for CBOB and CBOB:Pt the oxidation rates are significantly inhibited by SOD and catalase rather than carotene (Fig. 4*B* and *SI Appendix*, Fig. S12). Thus, the dominant ROS are $O_2^{\bullet -}$ and •OH, pointing to the electron

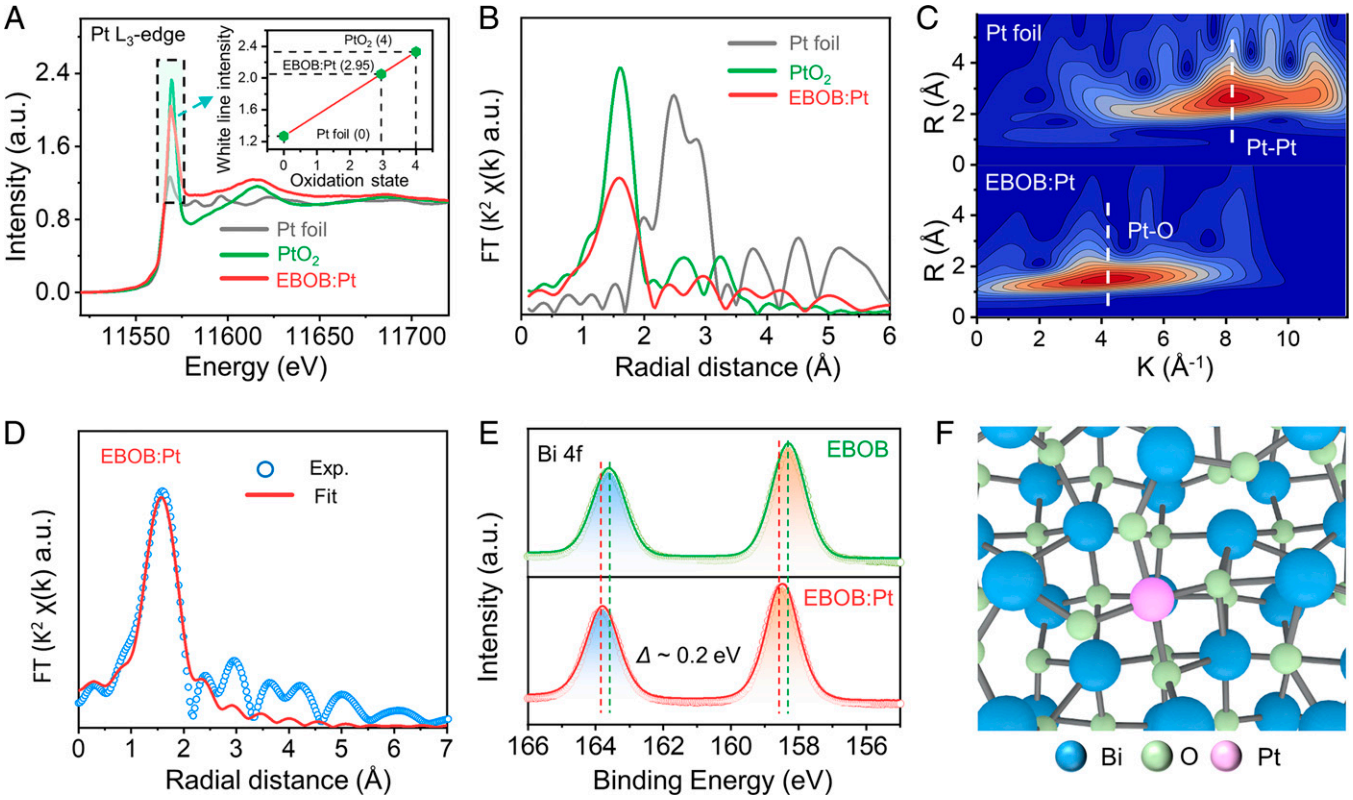

Fig. 3. XPS and synchrotron radiation XAFS characterizations. (*A*) Normalized Pt L_3-edge XANES spectra of EBOB:Pt, as well as Pt foil and PtO_2 references. (*Inset*) The average oxidation state of Pt in EBOB:Pt. (*B* and *C*) Corresponding FT-EXAFS spectra and WT-EXAFS plots from *A*. (*D*) FT-EXAFS fitting curves of EBOB:Pt. (*E*) Bi 4f XPS spectra of EBOB and EBOB:Pt. (*F*) Schematic atomic coordination model of EBOB:Pt. a.u., arbitrary units.

transfer behavior in CBOB and CBOB:Pt. Moreover, compared with EBOB and CBOB, the ROS over both EBOB:Pt and CBOB:Pt increase much faster, implying the role of Pt doping on the promotion of O_2 activation in different systems.

Electron spin resonance (ESR) measurements were carried out to gain more direct proof for the ROS in different systems. As illustrated in Fig. 4*C*, by using 2,2,6,6-tetramethyl-4-piperidinol-*N*-oxyl (TEMP) as the trapping agent, triplet peak signals (1:1:1, α_N = 16.9 G, g = 2.0054) of 2,2,6,6-tetramethyl-4-piperidinol-*N*-oxyl radical (TMPN) emerge, indicating the presence of $^1O_2$ in EBOB and EBOB:Pt (*SI Appendix*, Fig. S13). Not surprisingly, it is not detected in either CBOB or CBOB:Pt. Instead, when 5,5-dimethyl-1-pyrroline *N*-oxide (DMPO) was used as the trapping agent we observed the sextet peak signals of DMPO-OOH (α_N = 12.9 G, α_H =10.3 G, g = 2.0057, a spin adduct derived from DMPO- $O_2^{\bullet-}$) (Fig. 4*D*) and quadruple peak signals of DMPO-•OH (1:2:2:1, $\alpha_N = \alpha_H$ = 14.9 G, g = 2.0055) (*SI Appendix*, Fig. S14) in CBOB and CBOB:Pt systems, which are expected in charge-carrier-involved systems. On the contrary, they show negligible DMPO-OOH signals in both EBOB and EBOB:Pt systems. According to the different major ROS in different systems, we can confirm that the $^1O_2$ generation would be ascribed to the robust excitonic effect in EBOB, while the $O_2^{\bullet-}$ and •OH generation would be related to the hot carriers transfer in CBOB. Also, they can be used as model systems to study the role of Pt doing in exciton-involved and charge-carrier-involved photocatalysis, respectively. In addition, both EBOB and EBOB:Pt exhibit highly oxygen-dependent oxidation character, indicating the ROS are indeed associated with the activation of O_2 (Fig. 4*E*). Moreover, $^1O_2$ sensor green (SOSG), which can hardly react with ROS other than $^1O_2$ (23), can be used to further verify the production $^1O_2$ amount. The maximum fluorescence emission intensity of EBOB:Pt is about two times higher than that of EBOB (Fig. 4*F*), indicating that the Pt dopants on EBOB surface are responsible for the enhanced excitonic effect.

Insights into the Excitonic Regulation Mechanism in $^1O_2$ Generation. To uncover the underlying reasons for the improved O_2 activation, the fundamental steps in photocatalysis were investigated. *SI Appendix*, Figs. S15 and S16*A* display the N_2 adsorption/desorption isotherms and ultraviolet-visible (UV-vis) diffuse reflectance spectra of EBOB and EBOB:Pt (*SI Appendix*, Fig. S17 displays the information of CBOB and CBOB:Pt); obviously, the enhancement of $^1O_2$ generation cannot be easily interpreted by a little increased surface area and a little reduced band gap. To further disclose the excitonic effects in EBOB systems, photoluminescence measurements were conducted. The fluorescence (PF) is usually generated by the charge carrier recombination in charge-carrier-involved systems or radiative decay of singlet excitons in exciton-involved systems, while the phosphorescence (PH) stemmed from the triplet excitons, which is related to the transition from singlet to triplet state by ISC (24). As shown in Fig. 5*A*, the observation of PH clearly validates the existence of triplet excitons in the EBOB systems; however, CBOB systems show no PH signals at all. In addition, the distinguishable difference in PH intensity confirms a greatly enhanced triplet-exciton yield in EBOB:Pt with respect to EBOB, thus increasing the $^1O_2$ generation through triplet energy transfer. To evaluate the exciton binding energy (E_b), DFT calculations were conducted. According to the classical Mott–Wannier model, the E_b is proportional to the effective exciton mass $\mu_{ex} = m_e m_h/(m_e + m_h)$, where m_e and m_h represent the effective mass of electrons and holes. As shown in Fig. 5*B* and *SI Appendix*, Table S3, the μ_{ex} of the EBOB system is obviously larger than that of the CBOB system, which is

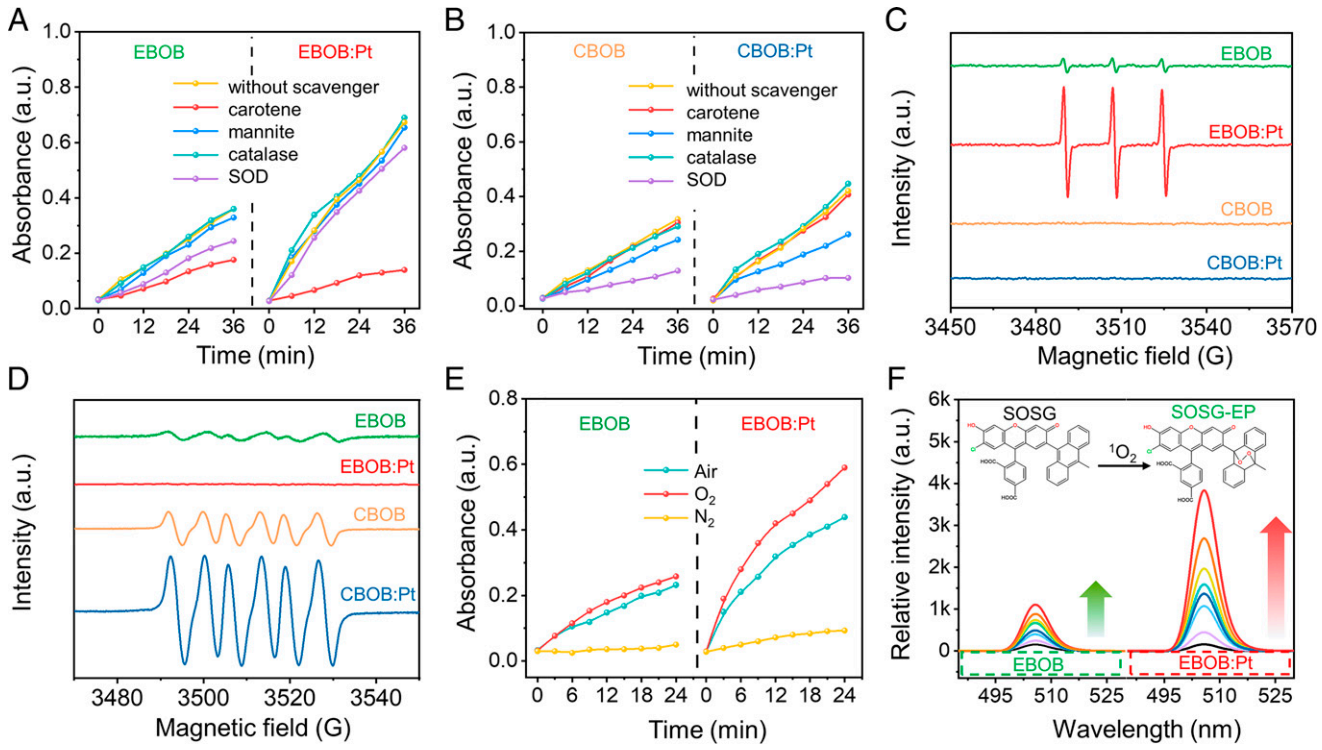

Fig. 4. Molecular oxygen activation properties and reactive intermediates identification. (*A* and *B*) UV-vis absorbance for TMB oxidation product monitored at 380 nm along with reaction time over EBOB and EBOB:Pt (*A*) and CBOB and CBOB:Pt (*B*) in the presence of different scavengers in O_2 atmosphere under visible light irradiation. (*C* and *D*) ESR spectra of EBOB, EBOB:Pt, CBOB, and CBOB:Pt in the presence of TEMP (*C*) and DMPO (*D*) in O_2 atmosphere under visible light irradiation. (*E*) UV-vis absorbance of TMB oxidation with EBOB and EBOB:Pt monitored at 380 nm under different gas conditions. (*F*) Time-dependent fluorescence intensity in the reaction of SOSG with $^1O_2$ generated from EBOB and EBOB:Pt in O_2 atmosphere under visible light irradiation. a.u., arbitrary units.

in accordance with the ROS species and PH results. Meanwhile, the E_b cannot be effectively tuned by te Pt doping, and thus it is not the main reason for the enhancement of excitonic effect in EBOB. Also, it should be noted that the DFT results of E_b only give a qualitative prediction, and not the true values.

To gain an in-depth understanding of the impact of Pt doping on exciton dynamics, a combination of femtosecond time-resolved transient absorption (TA) spectroscopy, PF and PH spectra, and DFT calculation is quite necessary, as they can give comprehensive information about the involved photophysical processes for the singlet–triplet conversion (25). Fig. 5*C* shows the TA spectra of EBOB and EBOB:Pt excited by 310-nm pulses, which contain a broad-band photoinduced absorption feature attributed to the excited-state absorption, consistent with a previous study (19). It is obvious that EBOB:Pt has a stronger absorption signal than EBOB, indicating the increased singlet exciton concentration of EBOB:Pt under the same irradiation condition, which is consistent with the increased UV-vis absorption. After the singlet exciton generation, the relaxation pathways can be confirmed on the basis of multiexponential fit and corresponding time constants (τ) of the TA kinetics at 650 nm (Fig. 5*D*). Clearly, EBOB:Pt exhibits a relatively shorter recovery lifetime of photoexcited excitons compared to EBOB, which would facilitate the ISC process for triplet-excitons generation. For EBOB, the observed biexponential relaxation pathways suggest typical excitonic processes: 1) an ISC process (τ_1 = 506.45 ps) of excitons converted from S_1 to T_1 with a change of spin-multiplicity and 2) the formed excitons in S_1 decay back to S_0 on a much longer lifetime (τ_2 = 3318.48 ps). Markedly, it turned out that the TA kinetics of EBOB:Pt can only be fitted by a triexponential decay function rather than a biexponential decay function, and the fitting results and corresponding time constants show three relaxation pathways: 1) a fast relaxation (τ_1 = 53.60 ps) of S_1 to impurity (Pt)-mediated TS and forming singlet excitons with lower energy level (S_1*); 2) an accelerated ISC process (τ_2 = 167.89 ps) of excitons converted from S_1* to T_1; and 3) the formed excitons in S_1 decay back to S_0 (τ_3 = 1852.18 ps).

The TA analyses highlight the role of Pt dopants on excitonic regulation; however, more specific evidence is needed to confirm the above hypothesis. We first performed ab initio calculations on the electronic structures of EBOB and EBOB:Pt using DFT to confirm the impurity states. Fig. 5*E* shows the density of states (DOS) plot for EBOB and EBOB:Pt. Upon Pt doping, the Pt atom in a Bi site provides an obvious impurity state in between the valence and conduction bands of EBOB. After photoexcitation (Fig. 5*F*), the photogenerated charges are localized into the Pt state, where the trap singlet excitons (S_1*) generate. To evaluate the ISC efficiency, the energy separations between the PF and PH peaks were measured (Fig. 5*G*), which can estimate the ΔE_{ST} values, i.e., 0.279 and 0.145 eV for EBOB and EBOB:Pt, respectively. Such a reduction of ΔE_{ST} by ~48% could effectively facilitate the ISC process and hence efficient triplet exciton generation, which is consist with the TA results. Moreover, the obviously weakened photoluminescence (PL) intensity and roughly twofold decrease of the mean PF lifetime (*SI Appendix*, Fig. S18) also suggest the acceleration of ISC and more effective conversion from singlet to triplet excitons. It is worth noting that the PF emission of EBOB:Pt does not show any shift compared to that of EBOB and no new PF emission peak forms, which means that the excitons in S_1* would not return to the ground state (S_0). Furthermore, the PH kinetics in *SI Appendix*, Fig. S19 show the energy transfer process of triplet excitons, and the relatively decreased triplet

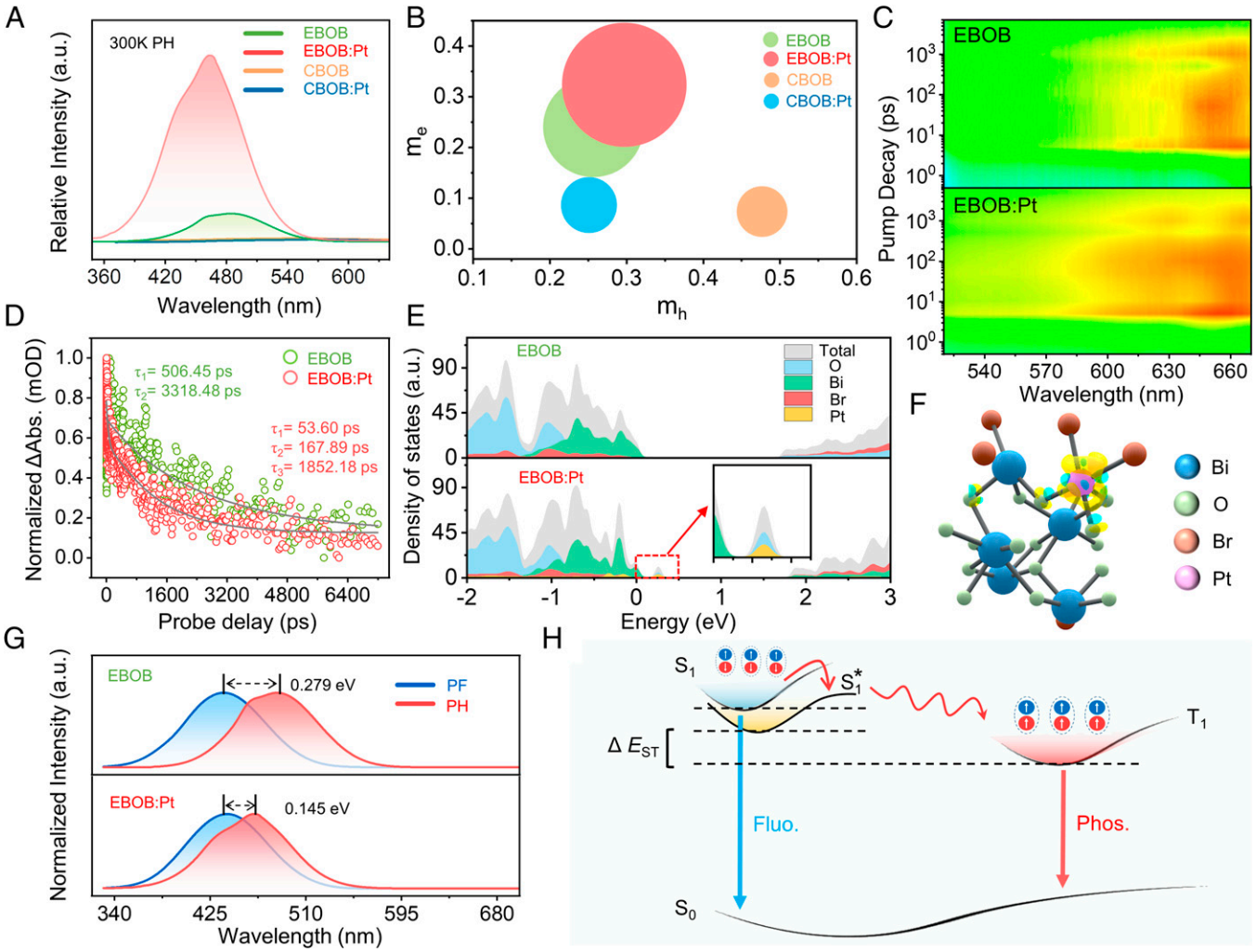

Fig. 5. Electronic structures of EBOB and CBOB by Pt doping. (*A*) Steady-state PH spectra of EBOB, EBOB:PT, CBOB, and CBOB:Pt obtained at 300 K. (*B*) The effective exciton mass μ_{ex} of EBOB, EBOB:PT, CBOB, and CBOB:Pt obtained by DFT calculations (the circular area represents the value of μ_{ex}). (*C* and *D*) TA spectra and TA kinetic traces probed at 650 nm for EBOB and EBOB:Pt. (*E*) Calculated DOS of EBOB and EBOB:Pt (inset is the enlarged area from the red dashed rectangle). (*F*) Charge density contour plots of EBOB:Pt (the yellow and blue area represents enrichment of the charge). (*G*) Normalized steady-state PF and PH spectra of EBOB and EBOB:Pt obtained at 300 K. (*H*) Plausible energy transfer processes for triplet-excitons generation in EBOB:Pt. a.u., arbitrary units.

lifetimes of EBOB:Pt can be ascribed to the enhanced spin–orbit coupling. Finally, all things considered together, we proposed a plausible mechanism that regulates excitonic process in organic ultrathin structures (Fig. 5*H*). The new formed impurity states in the electronic structure can act as the singlet excitons TS, and the singlet excitons in S_1* would efficiently reduce the ΔE_{ST} to accelerate the ISC process, thus more triplet excitons yield to undergo energy transfer for $^1O_2$ generation. Meanwhile, the mechanism of O_2 activation in charge-carrier-involved CBOB system has also been explored, and it only shows the traditional photocatalytic viewpoint (*SI Appendix*, Figs. S20–S22).

The transfer of triplet excitons from excited photocatalyst to O_2 is crucial for O_2 activation in exciton-triggering photocatalysis, and it might involve some quite nontrivial scenarios of energy transfer between photocatalysts and O_2 molecules. Accordingly, the bonding configurations between photocatalysts and O_2 would determine O_2 activation efficiency and mechanism (16). To determine the impact of surface structure on the O_2 activation, DFT calculations were employed. In the simulations, the adsorption state of O_2 on different sites was examined and the effects of the adsorption process on the spin state of electrons in O_2 were analyzed. Some bonding configurations were considered (*SI Appendix*, Fig. S23) and the most favorable configurations on EBOB and EBOB:Pt (001) surfaces are shown in Fig. 6 *A* and *B*. According to the adsorption energy, O_2 is more favorably adsorbed on EBOB:Pt surface, which is consist with the XPS results (*SI Appendix*, Fig. S24). Moreover, the magnetic moment of chemisorbed O_2 on EBOB:Pt is 0.013 μB, which is 1.987 μB lower than the free O_2 molecules (26). In contrast, the magnetic moment of chemisorbed O_2 on EBOB is 1.039 μB, which is 0.961 μB lower than O_2 and 1.026 μB higher than that of O_2 on EBOB:Pt (*SI Appendix*, Table S4). In terms of the decrease in the magnetic moment of O_2, the O_2 is more activated on EBOB:Pt. Importantly, the significant reduction of magnetic moment to nearly 0, indicating the perfect spin-flip process upon the chemisorption on EBOB:Pt. To further get deep insight into the energy transfer process, the calculated density difference for EBOB (e) and EBOB:Pt (e) (Fig. 6*C*) in the presence and absence of O_2 suggests that the significant electron transfer occurring on the EBOB:Pt surface should be the primary mechanism responsible for O_2 activation during the chemisorption. As is known, the magnetism of O_2 comes from the two nonpaired electrons in the frontier π* orbital (27), and the transferred electrons from EBOB:Pt surface to O_2 will

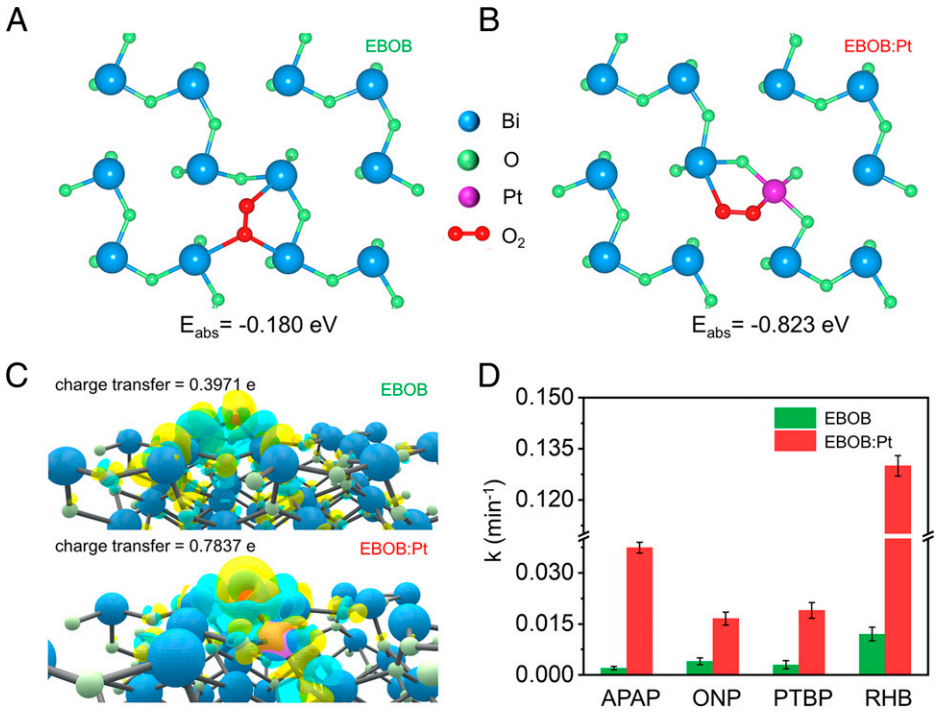

Fig. 6. Surface structures and organic degradation properties of EBOB and EBOB:Pt. (*A* and *B*) The most favorable adsorption configurations of O_2 on EBOB (*A*) and EBOB:Pt (*B*) (001) facets. (*C*) Calculated charge density difference for EBOB and EBOB:Pt. (*D*) Catalytic degradation properties of EBOB and EBOB:Pt for APAP, ONP, PTBP, and RHB.

occupy its antibonding π^* orbital, leading to the spin reduction on O_2, which confirms the electron-mediated triplet energy transfer process (28).

Inspired by the key role of excitonic regulation behavior between Pt and the Bi_3O_4Br nanosheet in the exciton-photocatalysis system in promoting $^1O_2$ generation, we were intrigued to find out whether other metal doping into Bi_3O_4Br can also possess a similar phenomenon and whether our method can be used for regulation in other systems with excitonic effects. First, we explored the Pd-doped Bi_3O_4Br material, which has similar properties to EBOB-Pt and enhances the activation of oxygen and the generation of singlet oxygen in the system (*SI Appendix*, Figs. S25, S27, and S29). In addition, we doped Pt in BiOBr, which is a material with exciton effect (19), and found results similar to the previously studied system (*SI Appendix*, Figs. S26, S28, and S30). Based on the above theoretical and experimental results, we believe that doping a small amount of metal in the materials of the two-dimensional exciton system may be a general method to enhance the exciton effect of the system and promote the generation of singlet oxygen.

In view of its high efficiency for $^1O_2$ generation, EBOB:Pt is expected to be a promising photocatalyst for water treatment applications, because $^1O_2$ is a primary oxidant for transformation of organic substances and inactivation of viruses in natural waters, especially for selective oxidative degradation of organic pollutants including polycyclic aromatic rings, chlorophenols, and pesticides (29–31). Indeed, Fig. 6*D* depicts that the EBOB:Pt photocatalyst can decompose multiple organic pollutants with diverse molecular structures, including acetaminophen (APAP), *o*-nitrophenol (ONP), *p*-tert-butylphenol (PTBP), and rhodamine B (RHB) (*SI Appendix*, Figs. S31–34). Moreover, the optimal EBOB:Pt with 0.7 wt % Pt doping exhibits effectively enhanced degradation rate with respect to EBOB, and it shows a high structural stability (*SI Appendix*, Fig. S35). Meanwhile, taking APAP as a model, the degradation pathway was studied in detail (*SI Appendix*, Fig. S36).

Discussion

In summary, we have demonstrated that restricting of electronic and surface structures of exciton-involved photocatalyst by introducing surface defects can effectively regulate the triplet-excitons yield and transfer for $^1O_2$ generation. As an example, Bi_3O_4Br one-unit-cell ultrathin layers with substitutional Pt dopants were successfully synthesized. Theoretical calculations suggest that introducing Pt dopants results in impurity states formation in between the valence and conduction bands, while TA, PF, and PH spectra show that the photoinduced excitons in S_1 can be trapped by impurity (Pt)-mediated TS and forming singlet excitons with lower energy level (S_1*), thus reducing ΔE_{ST} by ~48% and effectively facilitating the ISC process for efficient triplet-exciton yield. Moreover, the surface O_2 activation mechanism suggests that the optimal surface structure may alter the chemisorption state of O_2, and in turn, cause the changes in the magnetic moment (i.e., spin state) of O_2 through electron-mediated triplet energy transfer from Pt-doped Bi_3O_4Br surface to O_2. Thus, a spontaneous spin-flip process may occur during the chemisorption process, which facilitates $^1O_2$ generation. Benefiting from the highly specific $^1O_2$ generation, the modified Bi_3O_4Br exhibits excellent and selective oxidative degradation of organic pollutants in wastewater. This study develops understanding of the excitonic processes regulation in exciton-triggering photocatalysis.

Materials and Methods

Synthesis of the Pt-Bi_3O_4Br Atomic Layer. Solution A consisted of 0.5 mmol of $Bi(NO_3)_3{\cdot}5H_2O$ and 0.2 g polyvinylpyrrolidone (K30) was dispersed into 15 mL mannitol solution (0.1 mol/L) under stirring. Solution B consisted of 0.5 mmol NaBr dissolved into 3 mL mannitol solution (0.1 mol/L). Then, solution B was added dropwise to solution A under vigorous stirring. After stirring for 30 min, an NaOH solution (2 M) was used to adjust the pH of the above mixed solution to 11.5. After heating in an oven for 24 h at 160 °C the product was washed with deionized water and ethanol several times and dried. Then, 0.2 g product was dispersed into 60 mL ultrapure water (UP) for 20 min ultrasonically. H_2PtCl_6 solution (1.48 mg/mL) was added dropwise into the suspension

under vigorous stirring. The suspension was stirred for 2 h at 70 °C and then cooled to room temperature. The product was washed with UP and ethanol and dried in a 60 °C vacuum oven. The Pt contents were adjusted to 0, 0.3, 0.5, 0.7, and 1.0 wt %, which are named as EBOB, EBOB:Pt (0.3), EBOB:Pt (0.5), EBOB:Pt (0.7), and EBOB:Pt (1.0), respectively.

Synthesis of Bulk Pt-Bi_3O_4Br. A total of 3 mmol Bi_2O_3 and 3 mmol BiOBr was dispersed within 35 mL ethanol and stirred for 30 min at 30 °C. After the mixture was dried at 80 °C, the powder was calcined at 650 °C for 10 h in muffle with the ramping rate of 5 °C per min. The product was washed with deionized water and ethanol several times and dried. The loading method of Pt is the same as that of Pt-Bi_3O_4Br atomic layer. The Pt contents were adjusted to 0, 0.3, 0.5, 0.7, and 1.0 wt %, which are named as CBOB, CBOB:Pt (0.3), CBOB:Pt (0.5), CBOB:Pt (0.7), and CBOB:Pt (1.0), respectively.

Characterizations. The powder XRD was recorded on a Rigaku D/Max 2200PC X-ray diffractometer with Cu Kα radiation (λ = 0.15418 nm). The morphology was studied by SEM (Hitachi SU8010), high-resolution TEM (JEOL JEM-2100F), and HAADF-STEM energy-dispersive X-ray spectrometry (dual aberration correctors and four energy-dispersive X-ray spectroscopy [EDS] detectors, each of which has an effective area of 30 mm^2, were used to detect EDS signals). AFM images were recorded on a Bruker atomic force microscope under trapping mode. Raman spectra were collected on an RM1000 spectrometer with an Ar ion laser as excitation source. XPS was performed on a Thermal ESCALAB 250 electron spectrometer. The elemental content of the samples was determined through the ICP-MS (X7 Series; Thermo Electron Corporation). The optical absorption spectra were recorded on a UV-vis spectrophotometer (Shimadzu UV-2450) in the diffuse reflectance mode. In situ Fourier transform infrared was acquired using a THERMO Nicolet iS50. An electron paramagnetic resonance spectrometer (A300-10/12; Bruker) was used to observe the generated ROS. The steady-state fluorescence and phosphorescence spectra as well as the time-resolved phosphorescence spectra were collected on a FLS980 fluorescence spectrometer (Edinburgh Instruments Ltd.). Femtosecond Pump-Probe TA was detected by using Helios pump-probe system (Ultrafast Systems LLC) combined with an amplified femtosecond laser system (Coherent). The surface photovoltage was obtained on a CEL-SPS1000 surface photovoltage spectrometer (Beijing CEAULIGHT, Inc.),

X-Ray Absorption Spectroscopy Measurements. The X-ray absorption fine structure spectra (Pt L_3-edge) were collected at the 1W1B station in the Beijing Synchrotron Radiation Facility (BSRF). The storage rings of BSRF were operated at 2.5 GeV with a maximum current of 250 mA. Using Si (111) double-crystal monochromator, the data collection was carried out in transmission mode using an ionization chamber. All spectra were collected in ambient conditions.

Calculation Details. Spin-polarized DFT calculations were carried out with the Perdew–Burke–Ernzenhof exchange correlation functional and projector augmented wave pseudopotentials by using the Vienna Ab initio Simulation Package. A plane-wave energy cutoff of 500 eV was employed. The gamma-centered scheme K-points grid sampling was set at Γ point for all the calculations. All the structural relaxations were carried out until the residual forces were below 0.02 eV·$Å^{-1}$. A Heyd–Scuseria–Ernzerhof hybrid functional with ω = 0.2 $Å^{-1}$ was used to study the exact band gaps of samples. Within the framework of the Gaussian and plane wave methods, the unrestricted Kohn–Sham DFT was used as the electronic structure method.

Molecular Oxygen Activation Measurements. Fifty microliters of aqueous suspension of the sample (10 g·L^{-1}) and 20 μL of TMB (50 mM aqueous solution) were mixed with 2 mL of HAc/NaAc buffer solution. A 300-W Xe lamp equipped with a 420-nm cutoff filter was used as the light source. TMB oxidation was evaluated by UV-vis measurements (the absorbance around 370 nm) at different time intervals. To identify the type of active oxygen species, experiments were conducted at the same procedure with different types of scavengers.

Singlet Oxygen ($^1O_2$) Detection. SOSG was selected to detect the generated $^1O_2$. Typically, 20 mg of the sample is added to 60 mL of deionized water, under the irradiation of a Xe lamp with a 420-nm long-wavelength pass filter. During the illumination process, the mixture solution of 2-mL aliquots was collected at a given interval and then 2 μL SOSG (5 μM) was added. The $^1O_2$ generation can be estimated by PL intensity increase of the above mixture, where 504 and 525 nm were chosen as the excitation and emission wavelengths, respectively.

Photocatalytic Experiments. The photocatalytic performance evaluation of the samples was carried out by visible light-induced photodegradation of different organics (RHB, APAP, ONP, and PTBP). A 300-W Xe lamp (λ >420 nm) was used in the whole photodegradation process. Totally, 20 mg of catalyst was suspended into 100 mL pollutant (50 ppm RHB, 10 ppm APAP, 20 ppm PTBP, and 20 ppm ONP) solution with stirring for 30 min to establish adsorption–desorption equilibrium before light irradiation. Four-milliliter aliquots were collected at a given interval and centrifuged and then measured by a UV-vis spectrophotometer.

Photoelectrochemical Measurement. The electrochemical workstation (CHI760E; CH Instruments) was used for photoelectrochemical analysis in 0.5 M Na_2SO_4 solution using a conventional three-electrode system. The working photoanodes were made by depositing sample slurry (4-mg sample, 1 mL ethanol and 20 μL Nafion) on ITO glass (2.75 cm^2). The reversible hydrogen electrode (RHE) was obtained by converting the measured potential versus Ag/AgCl according to the Nernst equation: $E_{RHE} = E_{Ag/AgCl} + 0.197 + 0.059$ pH. Electrochemical impedance spectra were carried out in the frequency range of 0.05 to 10^5 Hz. For photoelectrochemical experiments, a 300-W Xe lamp equipped with a 420-nm cutoff filter was used as the light source.

Data Availability. All study data are included in the article and/or *SI Appendix*.

ACKNOWLEDGMENTS. We gratefully acknowledge financial support by the Natural Science Foundation of China as general projects (grants 22076082, 21874099, 22006029, and 21973091), Natural Science Foundation of Tianjin City of China (grant No. 17JCJQJC45000), the Tianjin Commission of Science and Technology as key technologies R&D projects (grants 19YFZCSF00740 and 20YFZCSN01070), Frontiers Science Center for New Organic Matter (grant 63181206), and the Youth Innovation Promotion Association, Chinese Academy of Sciences (grant 2021185).

1. X. Zhang *et al.*, Advances in photofunctional dendrimers for solar energy conversion. *J. Phys. Chem. Lett.* **5**, 2340–2350 (2014).
2. J. Gong, C. Li, M. R. Wasielewski, Advances in solar energy conversion. *Chem. Soc. Rev.* **48**, 1862–1864 (2019).
3. H. Wei, S. K. Loeb, N. J. Halas, J. H. Kim, Plasmon-enabled degradation of organic micropollutants in water by visible-light illumination of Janus gold nanorods. *Proc. Natl. Acad. Sci. U.S.A.* **117**, 15473–15481 (2020).
4. J. Luo *et al.*, A critical review on energy conversion and environmental remediation of photocatalysts with remodeling crystal lattice, surface, and interface. *ACS Nano* **13**, 9811–9840 (2019).
5. X. Jiao *et al.*, Fundamentals and challenges of ultrathin 2D photocatalysts in boosting CO_2 photoreduction. *Chem. Soc. Rev.* **49**, 6592–6604 (2020).
6. H. Wang *et al.*, Oxygen-vacancy-mediated exciton dissociation in BiOBr for boosting charge-carrier-involved molecular oxygen activation. *J. Am. Chem. Soc.* **140**, 1760–1766 (2018).
7. H. Wang *et al.*, Enhanced singlet oxygen generation in oxidized graphitic carbon nitride for organic synthesis. *Adv. Mater.* **28**, 6940–6945 (2016).
8. Y. Zhou *et al.*, Defect engineering of metal-oxide interface for proximity of photooxidation and photoreduction. *Proc. Natl. Acad. Sci. U.S.A.* **116**, 10232–10237 (2019).
9. S. Bai, N. Zhang, C. Gao, Y. Xiong, Defect engineering in photocatalytic materials. *Nano Energy* **53**, 296–336 (2018).
10. T. Yan *et al.*, Bismuth atom tailoring of indium oxide surface frustrated Lewis pairs boosts heterogeneous CO_2 photocatalytic hydrogenation. *Nat. Commun.* **11**, 6095 (2020).
11. X. Sun *et al.*, Enhanced superoxide generation on defective surfaces for selective photooxidation. *J. Am. Chem. Soc.* **141**, 3797–3801 (2019).
12. H. Li *et al.*, New reaction pathway induced by plasmon for selective benzyl alcohol oxidation on BiOCl possessing oxygen vacancies. *J. Am. Chem. Soc.* **139**, 3513–3521 (2017).
13. X. Wang *et al.*, Organic phosphors with bright triplet excitons for efficient X-ray-excited luminescence. *Nat. Photonics* **15**, 187–192 (2021).
14. H. Wang *et al.*, Ultrathin black phosphorus nanosheets for efficient singlet oxygen generation. *J. Am. Chem. Soc.* **137**, 11376–11382 (2015).
15. Y. Han *et al.*, Triplet sensitization by "self-trapped" excitons of nontoxic $CuInS_2$ nanocrystals for efficient photon upconversion. *J. Am. Chem. Soc.* **141**, 13033–13037 (2019).
16. Y. Qian, D. Li, Y. Han, H. L. Jiang, Photocatalytic molecular oxygen activation by regulating excitonic effects in covalent organic frameworks. *J. Am. Chem. Soc.* **142**, 20763–20771 (2020).
17. R. Long *et al.*, Surface facet of palladium nanocrystals: A key parameter to the activation of molecular oxygen for organic catalysis and cancer treatment. *J. Am. Chem. Soc.* **135**, 3200–3207 (2013).
18. J. Di *et al.*, Defect-tailoring mediated electron–hole separation in single-unit-cell Bi_3O_4Br nanosheets for boosting photocatalytic hydrogen evolution and nitrogen fixation. *Adv. Mater.* **31**, 1807576 (2019).
19. H. Wang *et al.*, Giant electron–hole interactions in confined layered structures for molecular oxygen activation. *J. Am. Chem. Soc.* **139**, 4737–4742 (2017).
20. J. Di *et al.*, Isolated single atom cobalt in Bi_3O_4Br atomic layers to trigger efficient CO_2 photoreduction. *Nat. Commun.* **10**, 2840 (2019).

21. Y. Yao *et al.*, Engineering the electronic structure of submonolayer Pt on intermetallic Pd_3Pb via charge transfer boosts the hydrogen evolution reaction. *J. Am. Chem. Soc.* **141**, 19964–19968 (2019).
22. K. Jiang *et al.*, Single platinum atoms embedded in nanoporous cobalt selenide as electrocatalyst for accelerating hydrogen evolution reaction. *Nat. Commun.* **10**, 1743 (2019).
23. D. J. Norman, A. Gambardella, A. R. Mount, A. F. Murray, M. Bradley, A dual killing strategy: Photocatalytic generation of singlet oxygen with concomitant Pt^{IV} prodrug activation. *Angew. Chem. Int. Ed. Engl.* **58**, 14189–14192 (2019).
24. H. Wang *et al.*, Insights into the excitonic processes in polymeric photocatalysts. *Chem. Sci. (Camb.)* **8**, 4087–4092 (2017).
25. L. Tian *et al.*, Overall regulation of exciton dynamics by defect engineering in polymeric photocatalysts for hydrogen evolution. *J. Phys. Chem. C* **124**, 24667–24676 (2020).
26. D. E. DeRosha, B. Q. Mercado, G. Lukat-Rodgers, K. R. Rodgers, P. L. Holland, Enhancement of C−H oxidizing ability in $Co-O_2$ complexes through an isolated heterobimetallic oxo intermediate. *Angew. Chem. Int. Ed. Engl.* **56**, 3211–3215 (2017).
27. Y. Nosaka, A. Y. Nosaka, Generation and detection of reactive oxygen species in photocatalysis. *Chem. Rev.* **117**, 11302–11336 (2017).
28. X. Luo *et al.*, Triplet energy transfer from perovskite nanocrystals mediated by electron transfer. *J. Am. Chem. Soc.* **142**, 11270–11278 (2020).
29. P. Liang *et al.*, An insight into metal organic framework derived N-doped graphene for the oxidative degradation of persistent contaminants: Formation mechanism and generation of singlet oxygen from peroxymonosulfate. *Environ. Sci. Nano* **4**, 315–324 (2017).
30. H. Kim *et al.*, Selective oxidative degradation of organic pollutants by singlet oxygen-mediated photosensitization: Tin porphyrin versus C_{60} aminofullerene systems. *Environ. Sci. Technol.* **46**, 9606–9613 (2012).
31. Z. Yang, J. Qian, A. Yu, B. Pan, Singlet oxygen mediated iron-based Fenton-like catalysis under nanoconfinement. *Proc. Natl. Acad. Sci. U.S.A.* **116**, 6659–6664 (2019).